Design, Sensing, and Control of a Magnetic Compliant Continuum Manipulator

Theodosia Lourdes Thomas, *Graduate Student Member, IEEE*, Jakub Sikorski, *Member, IEEE*, G. K. Ananthasuresh, Venkatasubramanian Kalpathy Venkiteswaran, *Member, IEEE*, and Sarthak Misra, *Senior Member, IEEE*

Abstract—Continuum manipulators coupled with magnetic actuation have great potential as steerable instruments for diverse surgical applications. They can be maneuvered inside the human body to reach difficult-to-access surgical sites with contactless actuation. This paper presents a new design of a compliant continuum manipulator of diameter 3 mm and length 70 mm, capable of spatial bending under magnetic actuation. A quasi-static model is developed to estimate the 3D motion of the manipulator. Experiments report an overall mean error in whole shape estimation of the manipulator between the model and the ground truth of 1.7 mm and 4.8 mm, when suspended vertically and horizontally from its base, respectively. Furthermore, fiber Bragg grating (FBG) sensors are integrated with the manipulator to enable shape sensing. Closed-loop control is demonstrated to trace different trajectories with the tip of the manipulator. A square trajectory and a straight line trajectory are generated with an average error in tip position of 4.1 mm between the desired and estimated positions. The potential of the manipulator as a steerable instrument is validated by maneuvering it inside phantoms of a bifurcating arterial system and a heart with visual guidance from a miniature camera.

Index Terms—Magnetic actuation, continuum manipulator, medical robotics, motion control, shape sensing.

I. INTRODUCTION

CONTINUUM manipulators have seen tremendous growth over the last few decades in various surgical applications such as laparoscopy, colonoscopy, neurosurgery and robot-assisted surgery among others [1]. A continuum manipulator is a continuously curving robotic device with several degrees of freedom (DoF). Miniaturized continuum manipulators can be designed to control their shape in 3D space and precisely steer inside the human body to reach difficult-to-access surgical sites. Recent advancements in the design of compliant mechanisms have resulted in various miniaturized flexible continuum manipulators with a wide range of motion [2]. Notched-tube compliant joint mechanisms in particular have gained significance in enhancing DoF and dexterity. Flexible manipulators having different patterns of triangular, rectangular and asymmetric notches have been explored to operate in single-port access surgeries [3], [4]. Such manipulators are known to have reduced stiffness and require careful optimization of the notch pattern to operate in confined spaces [5].

Accurate modelling of continuum manipulators is important in precisely maneuvering the manipulator to the surgical site. Constant curvature approximation is a commonly applied framework for continuum robots, but it can be challenging due to the error propagating from variable curvature robot shapes [6]. Cosserat-rod is a geometrically-exact model more generally used for soft manipulators, however it can be difficult to implement as it involves solving partial differential equations [7]. By contrast, rigid-link modelling is a simplified approach for approximating continuum manipulators with multiple DoFs as concatenated rigid links and flexible joints using well-established kinematic and dynamic models [8].

A common method of controlling continuum manipulators is using cable-driven actuation. Examples include commercially available systems like the Sensei X Robotic Catheter System by Hansen Medical Inc. (California, U.S.) and ViaCath system by BIOTRONIK (Berlin, Germany) [9]. Such systems require energy transfer through tendon coupling and can suffer from backlash and hysteresis. Recently, magnetic actuation is gaining interest in creating miniaturized manipulator designs as it enables manipulator control without the need for cables or tendons [10]. For instance, a 4 mm flexible catheter (NaviStar-RMT, Biosense Webster, Inc., California, USA) integrated with small permanent magnets, controlled using the Niobe magnetic navigation system (Stereotaxis Inc.,

Missouri, USA) and a motor drive (Cardiodrive, Stereotaxis, Inc., USA) is a leading technology for cardiovascular interventions [11]. Kratchman *et al.* demonstrated 3D tip trajectory planning of a magnet-tipped rod using Kirchoff elastic rod model in open-loop [12]. Model-based closed-loop control has been studied by many researchers using feedback of actuating wrenches [13], [14]. For instance, the first 3D closed loop control of a magnetic catheter was demonstrated by Edelmann *et al.* using Cosserat-rod model, however an external camera-based localization was implemented which is not clinically feasible [15].

Sensing the 3D shape of the manipulator in real-time while operating inside the body is quite challenging. Computed tomography (CT), magnetic resonance imaging (MRI) and ultrasound (US) imaging are widely used clinical imaging modalities for catheter tracking. However, these techniques have some limitations: CT leads to excessive X-ray exposure, MRI is not compatible with magnetic actuation and US has limited resolution inside the body [16]. Several studies have shown the virtues of using fiber Bragg grating (FBG) sensors in shape reconstruction of flexible medical instruments [17], [18], [19]. Optical fibers inscribed with FBG sensors are free from electromagnetic interference, thin, highly flexible and can be seamlessly integrated with medical instruments [20].

A new design of a monolithic metallic compliant manipulator capable of planar bending was presented in our previous proof-of-concept study [21]. This paper presents a novel design capable of spatial bending of the manipulator under magnetic actuation. This work validates the efficacy of the manipulator as a steerable surgical instrument with improved shape sensing and visualization capabilities over the previous study. The monolithic manipulator has a notched pattern of flexures with built-in mechanical motion constraints that limit the maximum stress in the flexures. A quasi-static model that uses rigid-link modelling is proposed to study the 3D motion of the manipulator when subjected to magnetic fields. Static experiments are conducted with the manipulator in an electromagnet setup (PaCMag), to analyse the proposed model. The shape sensing of the manipulator is improved by integrating an optical fiber inscribed with FBG sensors within the manipulator. A closed-loop control strategy is demonstrated in PaCMag to trace different trajectories with the tip of the manipulator. An observer-based fusion algorithm that fuses the tip pose information from the model and FBG sensors serves as feedback for the controller. The sensor fusion algorithm does not require external imaging like cameras or US imaging to estimate the tip pose of the manipulator [22], [23]. It has potential to offer a real-time visualization alternative to CT using X-rays.

The miniaturized manipulator presented is fabricated using a single tube of titanium, unlike most other manipulator designs reported in the literature that require assembly. The mechanical motion constraints in the design leads to distributed compliance, resulting in a safe manipulator by preventing the flexures from failing under stress. A comprehensive quasi-static model of the manipulator is developed which accounts for multiple DoFs, motion constraints, gravity and torsion. The 1 mm working channel of the manipulator enables integration of additional tools and sensors. The clinical feasibility of the manipulator is studied by carrying out experiments using a miniature camera (0.91 mm diameter) in phantom models of a bifurcating arterial system and a heart. Magnetic steering of the manipulator integrated with a miniature camera as feedback shows potential as a steerable catheter for endoscopy and ablation.

The rest of the paper is structured as follows: Section II begins with the description of the design and fabrication process of the manipulator. Section III introduces the quasi-static model developed to study the motion characteristics of the manipulator under magnetic actuation and is followed by the description of the test setup. Section IV details the three set of experiments with the manipulators comprising of static experiments, closed-loop control and clinical feasibility study. The inference and discussion on the results of the experiments are given in Section V. Finally, Section VI concludes the paper with a summary of this study and provides recommendations for future work.

II. THE COMPLIANT CONTINUUM MANIPULATOR

The compliant continuum manipulator is made by making cuts on a metallic tube to form two series of flexure pairs along the length of the tube. The two flexure pair series are oriented at 90° circumferential separation. The direction of cuts of one flexure pair series is reversed with respect to the other to make a compact design as shown in the isometric view of the manipulator in Fig. 1(a). Each flexure pair forms an elastic rotational joint that enables bending of the manipulator about the axis perpendicular to the longitudinal axis and the width of the flexure. A combination of the two series of flexure pairs oriented orthogonal with respect to each other results in the two-axis bending design. The range of motion of each flexure is physically constrained by the design geometry which also limits the maximum stress in the flexure to prevent failure.

A. Design

The design of the manipulator is shown in Fig. 1(a). It consists of two series of N flexure pairs distributed with 90° circumferential separation along the length (L) of the manipulator. The tube of the manipulator has inner radius (r) and outer radius (R). Each flexure is a thin plate of length (l), width (w) and thickness ($t = R - r$).

For design purposes, only the primary bending direction of the flexure is considered in the stress analysis as it is the predominant contributor to the stress. The total deflection of the manipulator is determined from the resultant sum of the deflections of each flexure pair ($\theta_i^{\max}$) while bending. In this design, $\theta_i^{\max}$ is limited by the width of the cut. It can be computed from geometry by assuming the axis of rotation is at the centre of the flexure. As shown in Fig. 1(d), point A in the wall of the manipulator makes first contact with the adjacent wall at point B. $\theta_i^{\max}$ is computed geometrically by the angle subtended by $\overline{AB}$ at the axis of rotation passing through O. Thus, the maximum deflection of the manipulator is calculated as follows

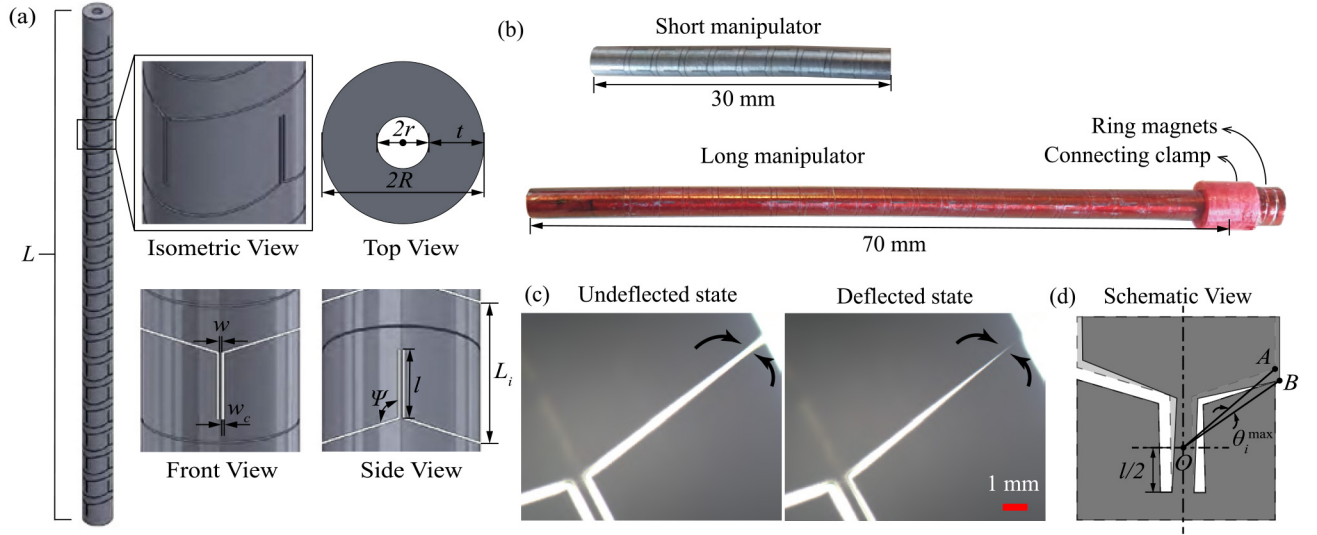$$\theta^{\max} = N\theta_i^{\max}. \tag{1}$$

Fig. 1. (a) The isometric, top, front and side views of two-axis bending design of manipulator with variables to define the design parameters. (b) Short and long versions of the manipulators fabricated using wire EDM. Three Neodymium ring magnets are connected to the long manipulator which is colored red for stereo vision tracking purposes. (c) Microscopic images of one flexure joint of the manipulator undergoing maximum deflection. (d) A schematic view of a flexure pair undergoing maximum deflection.

For safe operation of the manipulator without failure, the manipulator is designed such that the stress in each flexure does not exceed the yield stress of the chosen material (σ_y). Each flexure (i) experiences a maximum moment ($M_i^{\max}$) at a maximum deflection ($\theta_i^{\max}$) with respect to the preceding flexure ($i-1$) using Euler-Bernoulli beam theory [24] given by

$$M_i^{\max} = \frac{EI}{l}\theta_i^{\max}, \qquad (2)$$

where E is the elastic modulus of the material and the second moment of area of the flexure's cross section (I) given by $I = w^3 t/12$. The maximum stress in the flexure ($\sigma_{\max}$) and the factor of safety (FoS) is expressed as follows

$$\sigma_{\max} = \frac{M_i^{\max} w}{2I} = \frac{E\theta_i^{\max} w}{2l}, \qquad (3)$$

$$FoS = \frac{\sigma_y}{\sigma_{\max}}. \qquad (4)$$

Furthermore, the critical load for buckling (P_{cr}) is calculated using Euler's formula as follows:

$$P_{cr} = \frac{\pi^2 EI}{l^2}. \qquad (5)$$

This is the maximum axial load that the manipulator can safely carry without buckling. Similarly, the load capacities for bending and extension can also be calculated based on our previous work [21]. Bending will be the dominant effect and failure due to bending will only occur with fracture of the wall of the manipulator.

B. Fabrication

The manipulator is fabricated using a Titanium (grade-2) tube of outer and inner diameters of 3 mm and 1 mm, respectively. Titanium (grade-2) is chosen as the material as it has high ratio of yield strength to elastic modulus (σ_y = 345 MPa and E = 105 GPa) and low weight ratio. It is biocompatible

TABLE I
DESIGN PARAMETERS FOR TWO-AXIS BENDING DESIGNS OF SHORT MANIPULATOR ($N = 9$) AND LONG MANIPULATOR ($N = 21$) AS SHOWN IN FIG. 1(A), WHERE N IS THE NUMBER OF FLEXURES. LOAD CAPACITY FOR BENDING (F_{bend}), EXTENSION (F_{ext}), COMPRESSION (P_{cr}), AND FACTOR OF SAFETY (FoS) ARE ALSO GIVEN

Design Parameters		Load Capacity	
L	30 mm	F_{bend}	171.71 N
l	1.55 mm	F_{ext}	41.4 N
w	60 μm	P_{cr}	15.52 N
w_c	40 μm	FoS	7.13
ψ	100°		

and magnetically transparent. A series of flexure pairs is created along the length of the manipulator by making cuts using wire electrical discharge machining (EDM). Two manipulators of length 70 mm and 30 mm, henceforth known as the "long manipulator" and "short manipulator", respectively are fabricated as shown in Fig. 1(b) with design parameters and load capacities given in Table I. Prior to fabrication, a segment of the manipulator was analysed using finite element software (COMSOL Multiphysics 5.4). It was modelled using tetrahedral elements with minimum and maximum element size of 0.024 mm and 0.33 mm, respectively, in a stationary solid mechanics study. As shown in Fig. 2, the top end was constrained and the moment ($2M_i^{\max}$ = 5.8 x 10^{-5} Nm, because of two flexures) was applied to the bottom end about the two axes perpendicular to the longitudinal axis of the segment. This resulted in a maximum stress in the flexure of 50.9 MPa, which was validated with the stress calculated from the modelling approach Eqn. (3) giving 48.3 MPa with a factor of safety of 7.13.

III. MAGNETIC ACTUATION AND TEST SETUP

The manipulator is actuated using magnetic fields by means of a permanent magnet attached to its tip (Fig. 1(b)). The
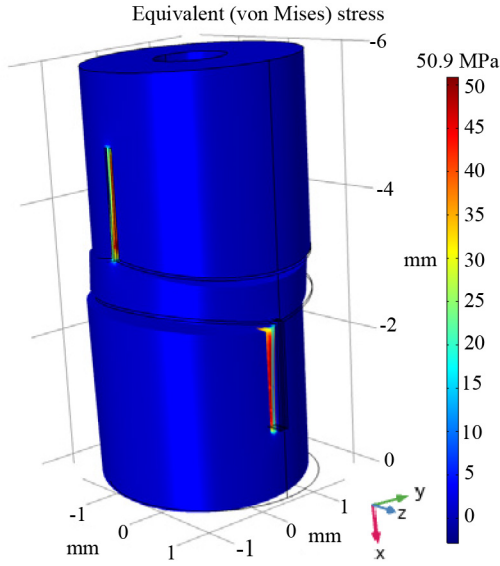
Fig. 2. Stress analysis of a single segment of the two-axis bending design using finite element software (COMSOL Multiphysics 5.4).
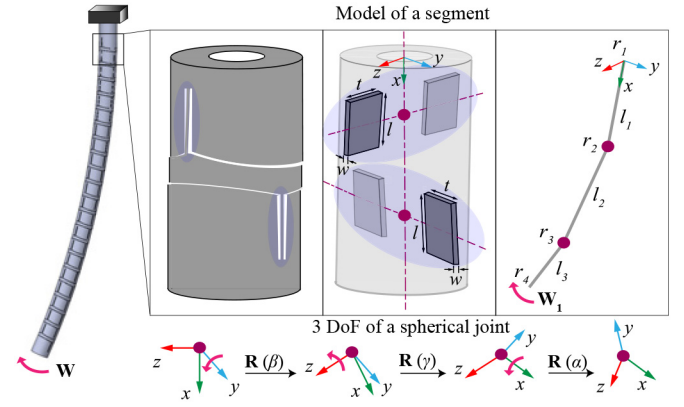

Fig. 3. A schematic of the quasi-static model of the manipulator made of N segments. Each segment is made of two flexure pairs, which are modelled as thin plates forming two spherical joints. Each spherical joint has three degrees of freedom (3-DoF) with three successive rotations $\mathbf{R}(\beta)$, $\mathbf{R}(\gamma)$ and $\mathbf{R}(\alpha)$, about x, y and z axes, respectively. The manipulator is fixed at one end and subjected to a load ($\mathbf{W}$) at its end. Each segment (i) is in static equilibrium with a load ($\mathbf{W}_i$) at its end.

manipulator is modelled using a rigid-body model to determine its configuration under the influence of external magnetic fields [25].

A. Quasi-Static Model

For the purposes of analysis, it is assumed that the manipulator undergoes quasi-static motion. The rigid-body model of the manipulator consists of N segments (Fig. 3). Each segment (S_k) taken in isolation is in static equilibrium with a load ($\mathbf{W}_k \in \mathbb{R}^6$) at its end. Each segment is composed of two orthogonally oriented flexure pairs. Each flexure pair is modelled as a spherical joint having three DoFs, with the axis of rotation located at the center of the flexure pair. Two DoFs correspond to the primary and auxiliary bending directions of flexure which are about the two axes perpendicular to the longitudinal axis, and the third DoF is due to the torsion about the longitudinal axis. Therefore, each segment consists of two spherical joints ($i \in \{2, 3\}$) at two points ($\mathbf{r}_i \in \mathbb{R}^3$) connecting three rigid links of given length ($l_i \in \mathbb{R}^+$, where $i \in \{1, 2, 3\}$). The three DoFs of the spherical joint (i) are the three rotational angles about x, y and z axes (α_i, β_i, $\gamma_i \in \mathbb{S}$). The corresponding rotational stiffnesses (K_{α_i}, K_{β_i}, $K_{\gamma_i} \in \mathbb{R}^+$) are calculated by approximating the flexure pair as two thin plates in parallel configuration, which gives

$$K_{\beta_i} = \frac{2EI_i^y}{l}, K_{\gamma_i} = \frac{2EI_i^z}{l}, K_{\alpha_i} = \frac{2GJ_i^x}{l}, \quad (6)$$

where E and G are the Young's modulus and shear modulus of the material. The second moment of area (I_i^*) and the polar moment of inertia (J_i^*) of the flexure pair (i) with the respective axes (*) are $I_2^y = I_3^z = \frac{w^3 t}{12}$, $I_2^z = I_3^y = \frac{w t^3}{12}$ and $J_i^x = I_i^y + I_i^z$, where l, w and t are the length, width and thickness of the flexure, respectively.

The internal joint torque ($\boldsymbol{\tau} \in \mathbb{R}^6$) of the rigid-body model is given by

$$\boldsymbol{\tau} = \begin{bmatrix} K_{\beta_2}\beta_2 & K_{\gamma_2}\gamma_2 & K_{\alpha_2}\alpha_2 & K_{\beta_3}\beta_3 & K_{\gamma_3}\gamma_3 & K_{\alpha_3}\alpha_3 \end{bmatrix}^T. \quad (7)$$

The load wrench ($\mathbf{W} \in \mathbb{R}^6$) acting at the end of the segment ($\mathbf{r}_4 \in \mathbb{R}^3$) in the spatial reference frame is defined as

$$\mathbf{W} = \begin{bmatrix} \mathbf{F} \\ \mathbf{M} \end{bmatrix} + \begin{bmatrix} 0_{3\times1} \\ \mathbf{r}_4 \times \mathbf{F} \end{bmatrix}, \quad (8)$$

where force ($\mathbf{F} \in \mathbb{R}^3$) and moment ($\mathbf{M} \in \mathbb{R}^3$) are associated with internal load (gravity) and external load (actuation). For static equilibrium, the following equation holds

$$\boldsymbol{\tau} = (\mathbf{J}_{\boldsymbol{\Theta}})^T \mathbf{W}, \quad (9)$$

where $\mathbf{J}_{\boldsymbol{\Theta}} \in \mathbb{R}^{6\times6}$ is the spatial manipulator Jacobian. Please refer to Appendix A for the detailed derivation. The above equation is a set of six nonlinear algebraic equations which can be solved to obtain the six DoFs (α_i, β_i, γ_i, where $i \in \{2, 3\}$) of a segment of the manipulator. This formulation can be extended for the entire manipulator having N 6-DoF segments with N loads acting at the respective ends. The static equilibrium equations for the entire manipulator using the rigid-body model are given by

$$\begin{bmatrix} \boldsymbol{\tau}_1 \\ \boldsymbol{\tau}_2 \\ \vdots \\ \boldsymbol{\tau}_N \end{bmatrix} = \begin{bmatrix} (\mathbf{J}_{\boldsymbol{\Theta}_1})^T & (\mathbf{J}_{\boldsymbol{\Theta}_1})^T & \cdots & (\mathbf{J}_{\boldsymbol{\Theta}_1})^T \\ 0 & (\mathbf{J}_{\boldsymbol{\Theta}_2})^T & \cdots & (\mathbf{J}_{\boldsymbol{\Theta}_2})^T \\ \vdots & \vdots & \ddots & \vdots \\ 0 & 0 & \cdots & (\mathbf{J}_{\boldsymbol{\Theta}_N})^T \end{bmatrix} \begin{bmatrix} \mathbf{W}_1 \\ \mathbf{W}_2 \\ \vdots \\ \mathbf{W}_N \end{bmatrix}, \quad (10)$$

where $\boldsymbol{\tau}_k$, $\mathbf{J}_{\boldsymbol{\Theta}_k}$, and $\mathbf{W}_k$ are the internal torques, Jacobian matrix and wrench associated with segment (S_k), respectively. Solving the above $N\times6$ system of equations gives the displacement of each flexure pair of the manipulator, and the position and orientation of the manipulator can be calculated using forward kinematics Eqn. (16).

B. Test Setup

The actuation of the manipulator is achieved using a magnetic actuation setup (PaCMag) as shown in Fig. 4. PaCMag consists of three pairs of electromagnetic coils which are situated orthogonal to each other to generate magnetic fields in
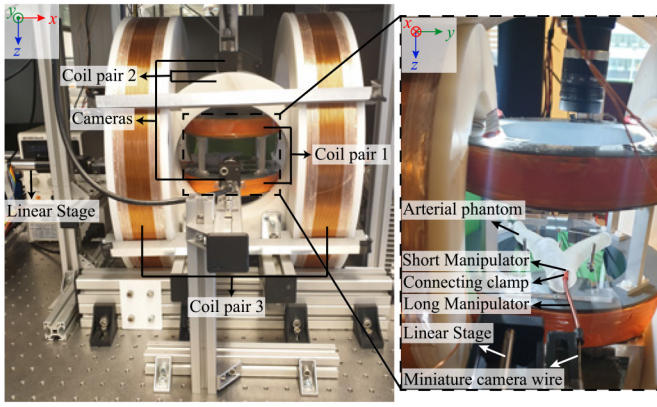
Fig. 4. PaCMag — an electromagnetic setup used for generating magnetic fields. The inset shows the insertion of the manipulator into a bifurcating arterial phantom using a linear stage.

3D space. The two coil pairs except for the coil pair 1 do not conform to the configuration of a Helmholtz coil pair. A magnetic field model for PaCMag is formulated based on Cartesian multipole expansion of a scalar potential that uses measurement-informed least squares optimization [26]. The current ($\mathbf{I} \in \mathbb{R}^3$) to field ($\mathbf{B^m} \in \mathbb{R}^3$) mapping is given by

$$\mathbf{B^m}(\mathbf{p}, \mathbf{I}) = \boldsymbol{\beta}(\mathbf{p})\mathbf{I}, \tag{11}$$

where $\boldsymbol{\beta}(\mathbf{p}) \in \mathbb{R}^{3 \times 3}$ is the unit-current field for position ($\mathbf{p} \in \mathbb{R}^3$) in PaCMag's reference frame. The inverse field map calculates the required currents to generate the magnetic field at any given position. The current in each coil pair is controlled by Xenus XE2-230-20 amplifiers (Copley Controls, Canton, USA). Each coil pair can independently generate a maximum magnetic field of 55 mT along its axis at the center of the workspace. PaCMag offers a cylindrical workspace of equal radius and height (65 mm). PaCMag is also equipped with two cameras placed orthogonal to each other, thus forming a stereo vision system to monitor the workspace.

Experiments with the long manipulator are performed by suspending it in the workspace of PaCMag. The base of the manipulator is fixed to a 3D printed support. N48 neodymium ring magnets (outer diameter = 4 mm, inner diameter = 1.5 mm, thickness = 1 mm, mass = 0.08 g and magnetic dipole moment = 0.012 Am^2) are attached to the end of the manipulator. Closed-loop control of the manipulator is performed with the integration of FBG sensors. A multi-core fiber inscribed with FBG sensors is used for this study [27] (Fig. 7). The multi-core fiber enclosed within a Hytrel furcation tubing (0.9 mm) is inserted into the 1 mm hole of the long manipulator. Additionally, an FBG-Scan 804D interrogator is installed to record the FBG sensor data.

To show clinical feasibility, experiments are conducted in 3D printed phantoms of a bifurcating arterial system and a heart. The manipulator is inserted using a linear slide (LX20, Misumi Group Inc., Tokyo, Japan), which is fixed horizontally at the base support. A miniature camera of 0.91 mm diameter (Misumi Electronic Corporation, Taiwan) integrated into the

TABLE II
RESULTS OF STATIC EXPERIMENTS IN VERTICAL AND HORIZONTAL CONFIGURATIONS FOR DIFFERENT TIP TRAJECTORIES: SQUARE AND LINE WITH SLOPE IN yz-PLANE (m) OF THE LONG MANIPULATOR WITH MAXIMUM STRENGTH OF MAGNETIC FIELD (B_{max}), THE ERROR BETWEEN QUASI-STATIC MODEL AND STEREO VISION MODELS FOR POSITION ($\Delta x, \Delta y, \Delta z$) OF THE MANIPULATOR TIP, AND MEAN WHOLE SHAPE ERROR ($\Delta \bar{d}$) ARE SHOWN IN TERMS OF MEAN VALUES AND STANDARD DEVIATION (IN BRACKETS)

Tip trajectory	B_{max} (mT)	Δx (mm)	Δy (mm)	Δz (mm)	$\Delta \bar{d}$ (mm)
Vertical Configuration					
Square	15	0.8 (0.6)	2.1 (1.4)	2.9 (1.4)	2.0 (0.5)
Square	10	0.7 (0.5)	2.0 (0.9)	2.3 (1.5)	1.8 (0.4)
Line: $m = \infty$	20	1.1 (0.5)	2.3 (1.1)	2.5 (1.2)	1.9 (0.3)
Line: $m = 0$	20	0.6 (0.4)	1.9 (1.3)	2.3 (1.1)	1.6 (0.2)
Line: $m = -1$	20	0.7 (0.6)	1.7 (0.8)	1.9 (1.2)	1.6 (0.3)
Line: $m = -1$	15	0.8 (0.6)	1.5 (0.9)	1.9 (1.3)	1.5 (0.3)
Horizontal Configuration					
Square	40	3.9 (2.1)	8.5 (5.8)	5.4 (4.6)	4.5 (1.6)
Square	25	4.0 (2.8)	10.5 (5.7)	5.8 (5.8)	5.4 (1.8)
Square	20	3.8 (2.5)	12.7 (5.3)	7.1 (5.6)	5.8 (1.6)
Line: $m = 0$	30	1.6 (1.5)	6.9 (5.7)	5.5 (4.8)	4.6 (1.2)
Line: $m = 0$	20	1.2 (0.9)	4.8 (1.9)	7.3 (4.2)	4 (1.1)

1 mm hole of the manipulator, is used as guidance to steer the manipulator.

IV. EXPERIMENTS AND RESULTS

This section presents the details of the different experiments carried out with the long and short manipulators. The first set of experiments is conducted to study the motion characteristics of the long manipulator under magnetic actuation. The second set of experiments demonstrates the closed-loop steering of the manipulator using tip pose feedback obtained from a sensor fusion algorithm. The final phase of the study comprises two experiments to show clinical feasibility. The combination of long and short manipulators is tested in 3D phantoms of a bifurcating arterial system and a heart guided by a miniature camera within the manipulators' working channel.

A. Static Experiments

Static experiments are performed inside PaCMag by suspending the long manipulator in two configurations: horizontally and vertically from its base. Two and three ring magnets are attached to the tip of the manipulator for the experiments in vertical and horizontal configurations, respectively. Time-varying magnetic fields are applied to generate different trajectories with the tip. A stereo vision setup is implemented to capture the shape of the manipulator based on 3D point cloud information followed by a fourth order 3D polynomial fitting along the length of the captured voxels of the manipulator [22]. Furthermore, the quasi-static model detailed in Section III-A is used to estimate the shape of the manipulator. The mean and standard deviation of errors between the quasi-static model and stereo vision data are presented in Table II. It shows the error in position of the tip of the manipulator and the mean whole shape estimation error which is calculated as the average of error in the position of N segments of the manipulator. The plots of the mean whole shape estimation error and the position of the manipulator tip are shown in Fig. 5. The overall mean error in whole shape estimation
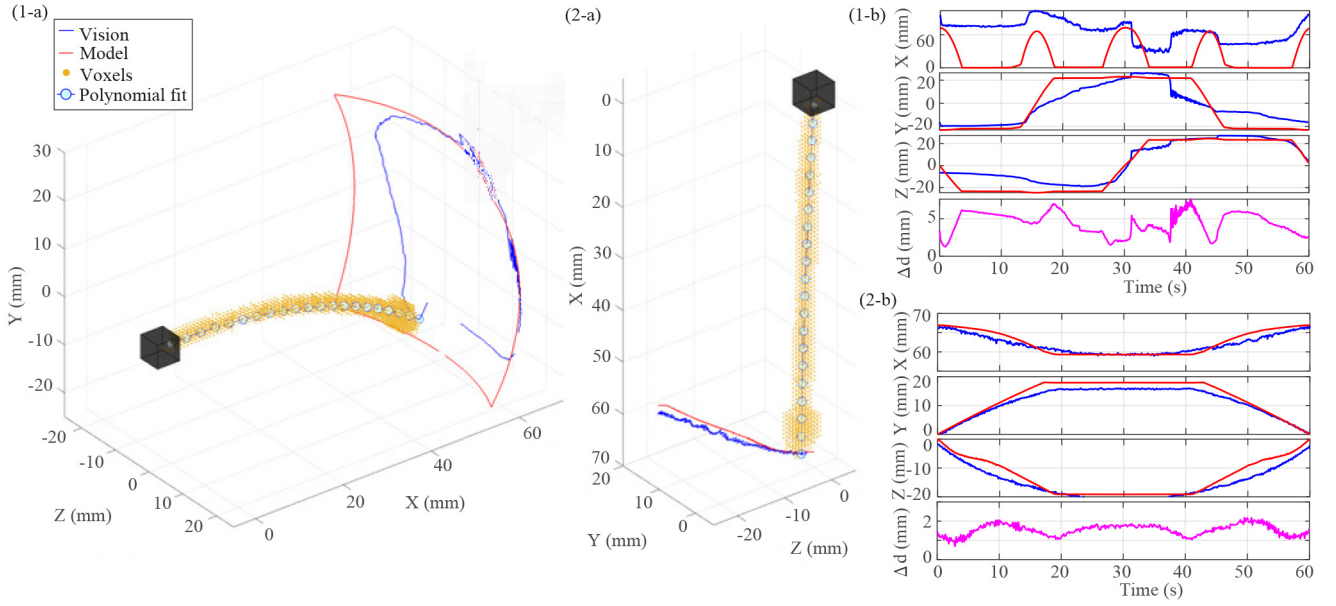
Fig. 5. Plots showing the captured voxels of the shape of the long manipulator, traced manipulator tip trajectory in *x*, *y* and *z*-coordinates, and the mean whole shape error (Δd) of the manipulator for the following experimental cases: (1) Square tip trajectory at $B_{max} = 40$ mT in horizontal configuration, (2) Line ($m = -1$) tip trajectory at $B_{max} = 20$ mT in vertical configuration.

between the model and stereo vision in vertical and horizontal configurations are 2 mm and 4.8 mm, respectively.

B. Closed-Loop Control

This study presents the closed loop control of the tip of the manipulator integrated with FBG sensors to trace different trajectories. The manipulator with two ring magnets at its tip is suspended horizontally in PaCMag and is subjected to magnetic torques. A proportional-integral (PI) controller is implemented to trace a desired trajectory with the tip of the manipulator as follows. Firstly, the pose of the manipulator tip is calculated using the quasi-static model. Additionally, the shape reconstruction technique with FBGs based on Bishop frames is used to calculate the pose of the manipulator tip [27]. Secondly, an observer-based fusion algorithm using Kalman state estimators fuses the aforementioned calculated poses from the quasi-static model and FBG model to obtain the estimated pose of the manipulator tip [23]. Thirdly, the torque necessary to correct the error between the estimated pose and desired pose of the manipulator tip is determined using a PI controller. The corresponding magnetic field is calculated using the torque and the estimated pose of the manipulator tip, that is, the ring magnets. Lastly, the inverse field map of PaCMag computes the required current which is supplied to the coils. The actuated manipulator is tracked by the stereo vision setup during the whole process. The pose measured by the stereo vision setup serves as the ground truth for the study. Fig. 6 is a block diagram summarizing the closed-loop control system.

1) FBG Shape Reconstruction: This section outlines the shape reconstruction technique using the multi-core fiber with FBG sensors integrated into the manipulator. Fig. 7 shows a schematic of the fiber. Four cores of the fiber, each with four

FBG sensors are used for shape reconstruction of the manipulator. The fiber is modelled as a regular unit-speed space curve in 3D space defined by curvature vectors and Bishop frame equations. The curvature vectors are calculated at the four FBG sensor sets using the strains computed from FBG wavelength measurements. Subsequently, the Bishop frame is used to derive the curve. Consequently, the pose of the manipulator tip is determined using the reconstructed shape of the manipulator. More details on this derivation can be found in the previous work [27].

Following the reconstruction technique, the fiber enclosed inside the manipulator is calibrated for this study by using data points obtained from open-loop experiments. The FBG shape reconstruction is registered with the ground truth shape obtained from the stereo vision. Fig. 7(b) shows the reconstructed tip position of the FBG sensors, quasi-static model and stereo vision. The overall mean error in tip position estimation between the FBG sensors and stereo vision is 4.86 mm and that between the quasi-static model and stereo vision is 6.86 mm.

2) Observer-Based Fusion: To improve the accuracy of the estimated pose of the manipulator tip, the pose data from the quasi-static model and FBG sensors are fused. The fusion of position and orientation of the manipulator tip are done separately using an observer-based sensor fusion algorithm in conjunction with Kalman state estimators. The estimated pose of the manipulator is obtained from the fused position ($\mathbf{p}^{\text{est}} \in \mathbb{R}^3$) and orientation ($\boldsymbol{\theta}^{\text{est}} \in \mathbb{S}^3$) computed as follows

$$\hat{\mathbf{x}}_{k+1|k+1} = \hat{\mathbf{x}}_{k+1|k} + \mathbf{K}_{k+1}\big[\mathbf{y}(k) - \mathbf{C}_d\hat{\mathbf{x}}_{k+1|k}\big], \quad (12)$$

where $\hat{\mathbf{x}}_{k|k}$ is the estimate of $\hat{\mathbf{x}}$ at time instant k given observations up to and including at time k, $\mathbf{K}_{k+1}$ is the optimal Kalman gain, $\mathbf{y}(k)$ is the measurement data from the model ($\mathbf{p}^{\text{Model}} \in \mathbb{R}^3$ and $\boldsymbol{\theta}^{\text{Model}} \in \mathbb{S}^3$) and FBG sensors ($\mathbf{p}^{\text{FBG}} \in \mathbb{R}^3$
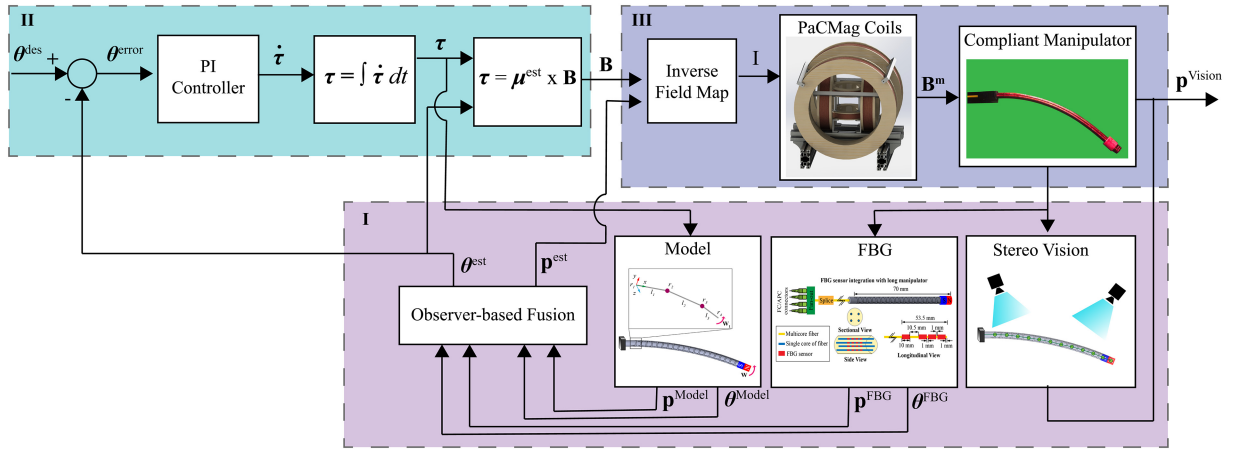
Fig. 6.　Closed-loop control system of the manipulator to trace different trajectories summarized in three blocks: (I) The pose of the manipulator tip is calculated by the quasi-static model ($\mathbf{p}^{\mathrm{Model}}$, $\boldsymbol{\theta}^{\mathrm{Model}}$) and the FBG sensors ($\mathbf{p}^{\mathrm{FBG}}$, $\boldsymbol{\theta}^{\mathrm{FBG}}$). An observer-based fusion algorithm fuses the two sets of data to calculate the estimated pose of the manipulator tip ($\mathbf{p}^{\mathrm{est}}$, $\boldsymbol{\theta}^{\mathrm{est}}$). The stereo vision system records the position of the manipulator tip ($\mathbf{p}^{\mathrm{Vision}}$), which serves as the ground truth. (II) A proportional-integral (PI) controller computes the torque rate ($\dot{\boldsymbol{\tau}}$) necessary to minimize the error ($\boldsymbol{\theta}^{\mathrm{error}}$) between the desired ($\boldsymbol{\theta}^{\mathrm{des}}$) and estimated ($\boldsymbol{\theta}^{\mathrm{est}}$) tip orientation. The associated magnetic torque ($\boldsymbol{\tau}$) is obtained by numerical integration of $\dot{\boldsymbol{\tau}}$. The corresponding magnetic field ($\mathbf{B}$) is obtained using the estimated magnet orientation ($\boldsymbol{\mu}^{\mathrm{est}}$). (III) The inverse field map of PaCMag determines the required current (I) for the coils to generate the reference magnetic field ($\mathbf{B}^{\mathbf{m}}$) and control the tip of the manipulator.
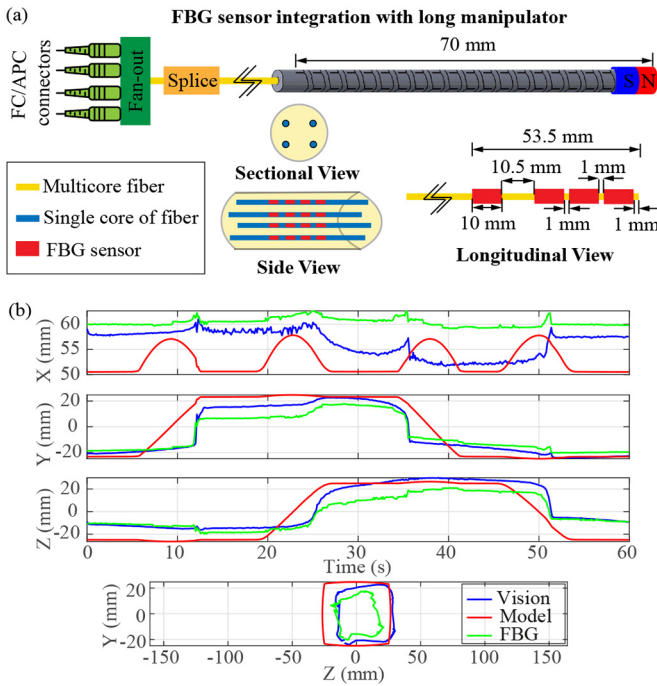

Fig. 7.　(a) A schematic of the multicore fiber with fiber Bragg grating (FBG) sensors integrated with the long manipulator. The side view depicts the four cores in blue, each with four FBG sensors in red. The section view depicts the orientation of the cores and the longitudinal view outlines the spacing of the FBG sensors in the fiber. (b) Plots of manipulator tip position obtained from FBG shape reconstruction (FBG), quasi-static model (Model) and stereo vision (Vision) after calibration.

and $\boldsymbol{\theta}^{\mathrm{FBG}} \in \mathbb{S}^3$) at time k, and $\mathbf{C}_d$ belongs to the disturbance dynamics measurement. More information on the above formulation is detailed in Appendix B and can be found in the previous work [23].

3) Proportional-Integral Control: The manipulator is actuated to follow a desired tip trajectory by implementing a PI

controller. The controller is designed to control the orientation of the manipulator about two axes (θ_y and θ_z), since no torque can be produced about the axis parallel to the direction of the magnetic dipole ($\boldsymbol{\mu}^{\mathrm{est}}$). The torque ($\boldsymbol{\tau} \in \mathbb{R}^3$) necessary to minimize the error ($\mathbf{e} \in \mathbb{S}^3$) between the desired tip orientation ($\boldsymbol{\theta}^{\mathrm{des}} \in \mathbb{S}^3$) and estimated tip orientation ($\boldsymbol{\theta}^{\mathrm{est}} \in \mathbb{S}^3$) is calculated as follows

$$\dot{\boldsymbol{\tau}} = K_P, \mathbf{e} + \int K_I, \mathbf{e} dt, \tag{13}$$

where $\mathbf{e} = \boldsymbol{\theta}^{\mathrm{des}} - \boldsymbol{\theta}^{\mathrm{est}}$, K_P and K_I are the PI gains. The corresponding magnetic control torque ($\boldsymbol{\tau}$) is obtained by the numerical integration of $\dot{\boldsymbol{\tau}}$. The associated magnetic field ($\mathbf{B}$) is determined for the current estimated magnet orientation ($\boldsymbol{\theta}^{\mathrm{est}}$) using the inverse of the equation below

$$\boldsymbol{\tau} = \boldsymbol{\mu}^{\mathrm{est}} \times \mathbf{B}, \tag{14}$$

where $\boldsymbol{\mu}^{\mathrm{est}}$ is the estimated magnetic dipole moment. The obtained magnetic field ($\mathbf{B} \in \mathbb{R}^3$) is transformed to the reference frame of PaCMag ($\mathbf{B}^{\mathbf{m}} \in \mathbb{R}^3$) in order to find the necessary current to be supplied by the coils. In this way, the inverse field map using Eqn. (11) calculates the required currents to generate the magnetic field ($\mathbf{B}^{\mathbf{m}}$) at the current estimated position ($\mathbf{p}^{\mathrm{est}}$) of the manipulator tip.

4) Results: Closed-loop control of the manipulator tip traces two trajectories: square and straight line. The poses of the manipulator tip calculated by the FBG sensors, quasi-static model, fusion and the stereo vision, and the applied magnetic torques are recorded during the experiment as plotted in Fig. 8. For the square and straight line trajectories, results show the average errors between the desired and estimated positions from fusion of 5.3 mm and 2.9 mm, respectively and that between the desired and stereo vision measured positions of 6.8 mm and 6.7 mm, respectively in position. The average error between the desired and estimated orientations from fusion of the square and straight line trajectories are 11.1° and
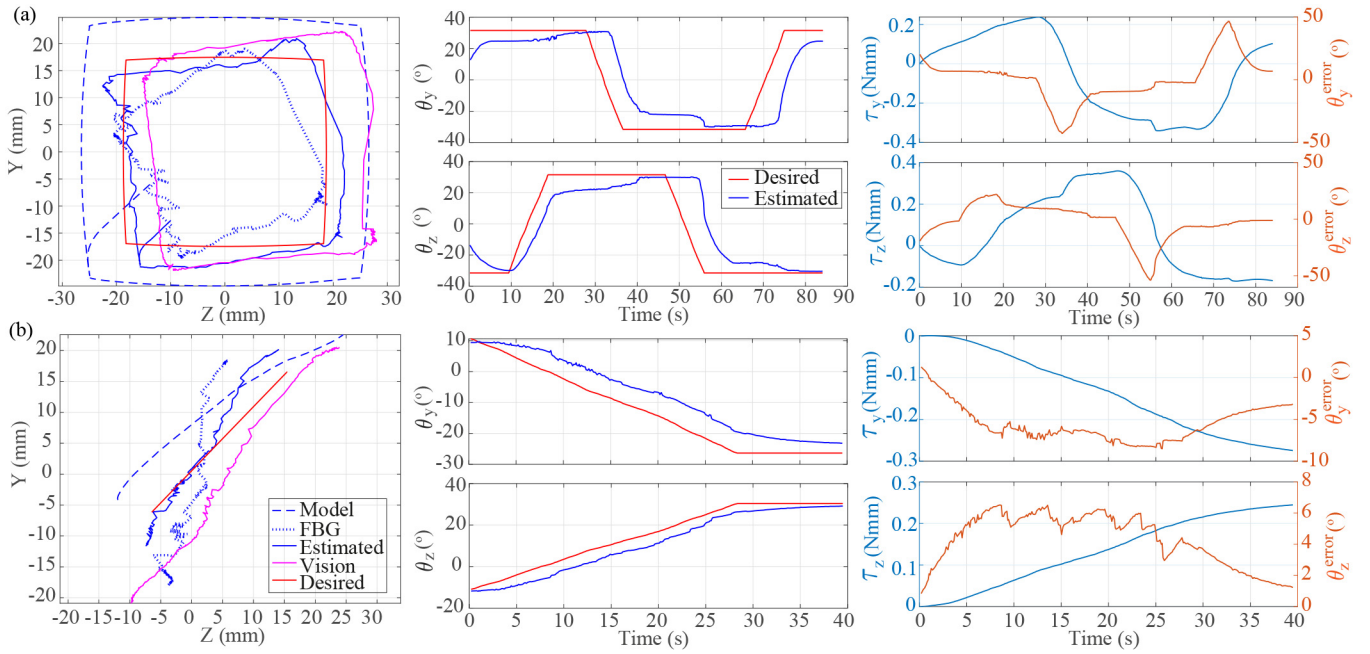
Fig. 8. Plots of closed-loop control experiments showing the position (y,z-coordinates) and orientation (θ_y, θ_z) of the manipulator tip, and magnetic torque (τ_y,τ_z) generated to correct the error in orientation ($\theta_y^{error}, \theta_z^{error}$), for two trajectories: (a) Square (b) Straight line.

4.8°, respectively. The tip orientation control implemented has a control frequency of 6.5 Hz.

C. Clinical Feasibility Study

These experiments demonstrate the maneuverability of the manipulator suspended in horizontal configuration inside two clinically relevant phantoms. A combination of the long and short manipulators forming a total length of 100 mm is used to cover a larger workspace. Two ring magnets are attached to its tip. The manipulator is inserted using a linear stage and steered in 3D by rotating the magnetic field to create different shapes and maneuver to target locations. A miniature camera integrated into the manipulator provides the visualization of the environment to navigate the manipulator in a clinically-relevant manner.

In the first experiment, the manipulator is accurately guided inside the undulating tapered channels of a bifurcating arterial phantom. The experiment is performed by positioning the phantom in vertical and horizontal orientations as shown in Fig. 9 (a-b). In the second experiment, the maneuverability of the manipulator is tested inside a heart model. The manipulator is inserted through the aortic valve and is guided to reach three targets locations in the left ventricle (Fig. 9(c)). By incorporating the miniature camera and increasing the length of the manipulator, these experiments demonstrate the steerability of the manipulator without relying on an external imaging system. Please refer to the video supplementary material for demonstration of the experiment results.

V. Discussion

The monolithic design of the manipulator makes it easy to fabricate from a single tube of titanium without requiring assembly. The 1 mm hollow interior channel offers room for embedding sensors to enhance its functionality. The flexure pair deflection is limited by the contact between the adjacent walls. The stress experienced by the flexures is below the designed threshold. This has led to a reliable and safe design without any noticeable plastic deformation even after repeated testing, as compared to the single-axis bending designs previously fabricated [21]. However, the maximum deflection of the long manipulator is observed to be 40°. The deflection can be increased by eliminating the contact between adjacent walls and enabling deflection until the flexures make contact with the adjoining wall. This redesign will require further optimization of the associated design parameters (l, w, w_c, ψ) of the manipulator.

Results of the static experiments with the long manipulator show that the quasi-static model is more accurate in the vertical configuration than the horizontal configuration experiments. This could be due to the difference in the effect of gravity. In vertical configuration, all the flexures experience gravity in the same direction, while in horizontal configuration the two sets of flexure pairs in the orthogonal planes experience gravity in different (local) bending directions. Therefore, in the subsequent closed-loop control demonstration, the manipulator was fixed at the base such that the flexure pairs are oriented 45° with respect to the direction of gravity for uniformity.

FBG sensors are introduced into the long manipulator to improve shape estimation of the manipulator. The accuracy of the FBG shape reconstruction is limited by the small curvature of the manipulator measured by only four sets of FBG sensors. The twisting of the fiber relative to the manipulator could also be a cause of error, since the fiber is only secured at its base and inserted in the hollow channel of the manipulator. The stereo vision system used as ground truth is also prone to
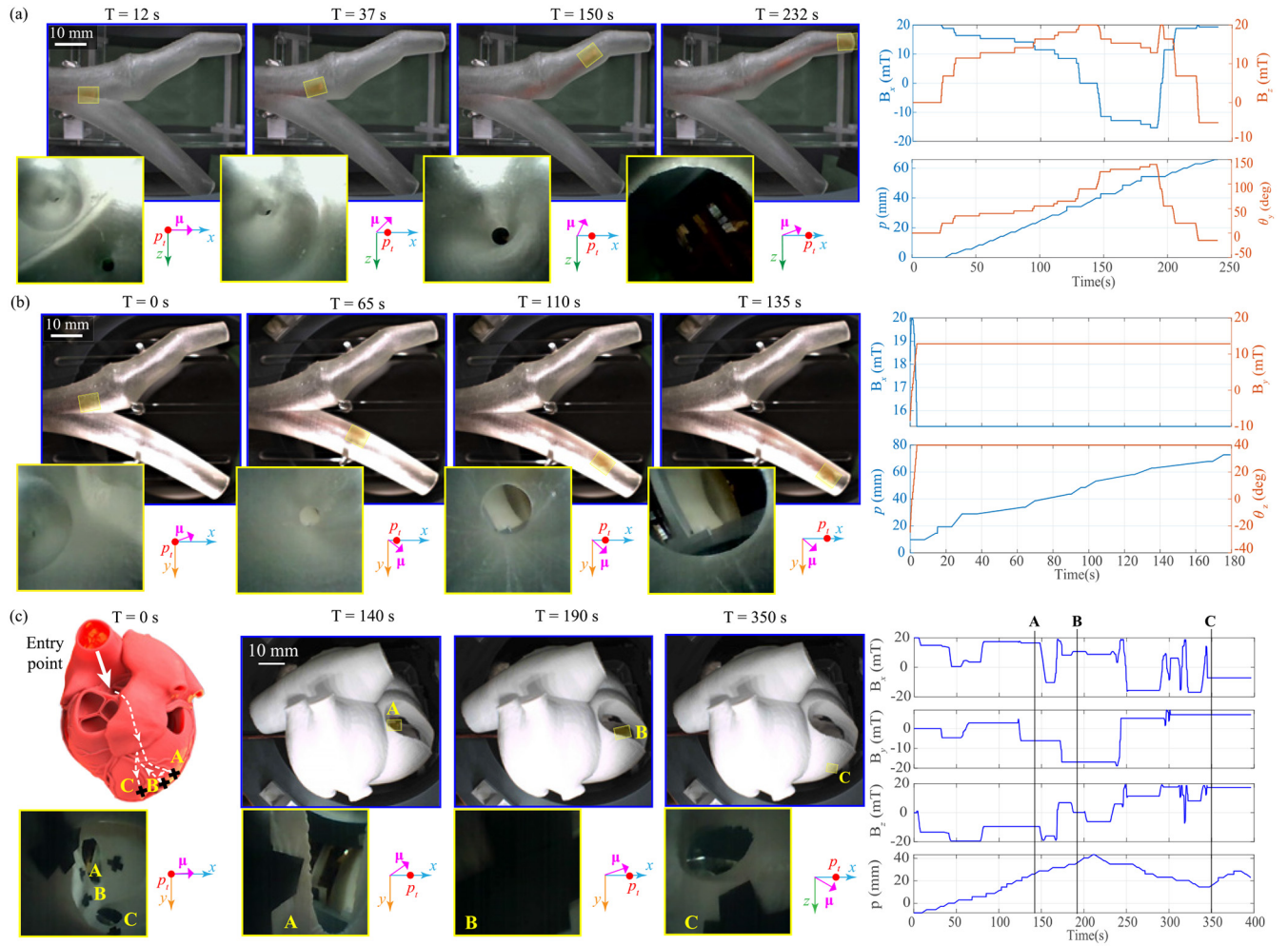
Fig. 9. Results of the clinical feasibility study: (a-b) Manipulator guidance inside a bifurcating arterial phantom suspended vertically and horizontally in the workspace of PaCMag. (c) Manipulator guidance inside a heart model placed in PaCMag. The dotted white lines show the traced trajectory starting at the aortic valve to reach three target locations A, B and C in the left ventricle. For all the experiments, the views of the miniature camera at the tip of the manipulator (highlighted in yellow) are shown at different time instants. Plots show generated magnetic field (B_x, B_y, B_z), its direction (θ_y, θ_z), and position of the linear stage (p). Please refer to the video supplementary material for the complete demonstration.

calibration error. Owing to the large length to diameter ratio of the manipulator, some distortion is observed in the images captured by the cameras.

The calibration results for shape sensing indicate that the tip position estimation using either the FBG sensors or the quasi-static model have errors greater than 3 mm (diameter of the manipulator) as shown in Fig. 7(b). It is observed that the FBG shape reconstruction underestimates the curvature and the quasi-static model overestimates the curvature. Therefore, an observer-based sensor fusion algorithm is implemented to improve the sensing results. This approach has been found to be the best among other multi-sensor fusion algorithms of unscented Kalman filter, Luenberger and Kalman state estimators investigated in our previous work [23], [28], [29].

For closed-loop control, orientation control of the manipulator tip (θ_y, θ_z) is chosen over position control, since position control becomes computationally expensive using the Jacobian of the manipulator. This can be simplified by reducing the DoFs per segment in the quasi-static model, as the deflection due to torsion and auxiliary bending are not significant

compared to primary bending deflection. Although the shape reconstruction using FBG sensors works reasonably well in open-loop (Fig. 7(b)), noise is observed during closed-loop (Fig. 8). This could be attributed to the low stiffness of the flexures which influences the dynamics of the manipulator during closed-loop motion, which in turn affects the performance of the sensor fusion algorithm. However, the controller follows the desired trajectory for the most part as inferred from the orientation plot of tip (Fig. 8). Higher error is seen during periods of motion with rapid transitions, like in square trajectory when transitioning from one edge to another. Straight line trajectory has relatively lower error due to the lower rate of changing angles. Though all the experiments are conducted assuming constant room temperature, temperature feedback can be added to the control system by incorporating a temperature sensor. For example, an additional FBG sensor can be embedded in the manipulator which does not experience any strain and measures the temperature.

The clinical feasibility study is carried out by combining the long and short manipulators in order to reach more locations in

the workspace. The ability of the manipulator to be precisely steered through a bifurcating artery phantom and reach specific target locations inside a heart phantom with the guidance of a miniature camera demonstrates potential applications in angioplasty, endoscopy and catheter ablation. The size of the manipulator is comparable to the $6 - 10$ Fr Magellan robotic catheters which are of outer diameters $2 - 3.33$ mm [30]. The maximum deflection of the combined manipulator is limited to $57°$, whereas the bending angle of steerable catheters can be between $45 - 180°$, up to $270°$ or even $360°$ depending on the application. There is a definite need to improve the positioning accuracy of the manipulator which is crucial in surgical procedures like ventricular tachycardia, where multiple lesions can be found at adjacent distances of the order of 5-10 mm [31].

VI. CONCLUSION AND FUTURE WORK

This paper presents a new design of a monolithic compliant continuum manipulator with a novel notched-tube pattern of flexures that ensures the stresses experienced are within design limits. Two versions of manipulator of lengths 70 mm and 30 mm capable of spatial bending up to $40°$ and $17°$, respectively, are fabricated using a single titanium tube of diameter 3 mm. The combination of the two can bend up to $57°$. A quasi-static model is developed to study the 3D motion of the manipulator under magnetic actuation. Static experiments show overall mean errors between whole shape estimated by the model and the ground truth of 1.7 mm and 4.8 mm, in horizontal and vertical configurations respectively. In order to improve the accuracy of shape estimation, an observer-based sensor fusion algorithm using Kalman state estimators is implemented with the integration of FBG sensors. The fusion algorithm has potential in offering a real-time visualization alternative to X-ray exposure during operation. Thereafter, a closed-loop control strategy to trace a square and a straight line tip trajectories is demonstrated, resulting in an average error between the desired and estimated tip positions of 4.1 mm. The feasibility of the continuum manipulator as a steerable catheter is studied by incorporating a miniature camera within its working channel, to show potential applications in endoscopy and catheter ablation. The accurate maneuvering of the manipulator in 3D to reach different target locations is demonstrated in two clinically relevant phantoms of a bifurcating artery and a heart.

In future work, the design of the manipulator will be improved to achieve higher range of motion ($> 90°$). Fabrication of complex shape profiles of flexures will be explored using wire EDM, electrochemical etching and laser cutting methods. Redesigning using a combination of segments of the manipulators connected by magnets with different polarities will be investigated. The dexterity and maneuverability will be improved by incorporating additional translation and rotational DoFs to the manipulator during insertion. The positioning and steering accuracy will be addressed by improving the shape sensing of the manipulator. Multiple FBG sensors will be embedded more securely along the length of the manipulator, and helical core fibers will be used to account for twist [32]. Control of the manipulator in tandem with medical imaging techniques and human-in-the-loop operation strategies will be explored. Further testing will be carried out in *ex-vivo* animal studies.

APPENDIX A
SPATIAL MANIPULATOR JACOBIAN CALCULATION

This section presents the procedure to calculate the spatial manipulator Jacobian for the rigid-body model of the manipulator described in Section III-A. Each spherical joint (i) undergoes three angular deformations: β_i, γ_i and α_i. Assuming the transformation matrix ($\mathbf{T}_i^{i+1}$) from joint (i) to joint ($i+1$) is defined as

$$\mathbf{T}_i^{i+1} = \begin{bmatrix} c_{\beta_i}c_{\gamma_i} & s_{\alpha_i}s_{\beta_i}-c_{\alpha_i}c_{\beta_i}s_{\gamma_i} & c_{\alpha_i}s_{\beta_i}+c_{\beta_i}s_{\alpha_i}s_{\gamma_i} & l_i c_{\beta_i}c_{\gamma_i} \\ s_{\gamma_i} & c_{\alpha_i}c_{\gamma_i} & -c_{\gamma_i}s_{\alpha_i} & l_i s_{\gamma_i} \\ -c_{\gamma_i}s_{\beta_i} & c_{\beta_i}s_{\alpha_i}+c_{\alpha_i}s_{\beta_i}s_{\gamma_i} & c_{\alpha_i}c_{\beta_i}-s_{\alpha_i}s_{\beta_i}s_{\gamma_i} & -l_i c_{\gamma_i}s_{\beta_i} \\ 0 & 0 & 0 & 1 \end{bmatrix}^T,$$

(15)

where c_* and s_* represent the cosine and sine of angle (*). Note that the first link (l_1) is rigidly attached to the base frame at point ($\mathbf{r}_1$), hence $\beta_1 = \gamma_1 = \alpha_1 = 0$. The position coordinates of each joint (i) are computed as

$$\begin{bmatrix} \mathbf{r}_i \\ 1 \end{bmatrix} = \prod_{j=1}^{i-1} \mathbf{T}_j^{j+1} \cdot \begin{bmatrix} \mathbf{r}_1 \\ 1 \end{bmatrix}^T,$$

(16)

The position vector ($p_* \in \mathbb{R}^3$) and the rotation axis ($\omega_* \in \mathbb{R}^3$) of spherical joint ($i$) are given by

$$\mathbf{p}_{\beta_i} = \begin{bmatrix} l_{i-1} & 0 & 0 \end{bmatrix}^T, \mathbf{p}_{\gamma_i} = \begin{bmatrix} 0 & 0 & 0 \end{bmatrix}^T, \mathbf{p}_{\alpha_i} = \begin{bmatrix} 0 & 0 & 0 \end{bmatrix}^T.$$ (17)

$$\boldsymbol{\omega}_{\beta_i} = \begin{bmatrix} 0 & 1 & 0 \end{bmatrix}^T, \boldsymbol{\omega}_{\gamma_i} = \begin{bmatrix} 0 & 0 & 1 \end{bmatrix}^T, \boldsymbol{\omega}_{\alpha_i} = \begin{bmatrix} 1 & 0 & 0 \end{bmatrix}^T.$$ (18)

The geometric twist between two successive DoFs is calculated using the above equations as follows

$$\boldsymbol{\xi}_{\beta_i} = \begin{bmatrix} \mathbf{p}_{\beta_i} \times \boldsymbol{\omega}_{\beta_i} \\ \boldsymbol{\omega}_{\beta_i} \end{bmatrix}^T = \begin{bmatrix} 0 & 0 & l_{i-1} & 0 & 1 & 0 \end{bmatrix}^T,$$ (19a)

$$\boldsymbol{\xi}_{\gamma_i} = \begin{bmatrix} \mathbf{p}_{\gamma_i} \times \boldsymbol{\omega}_{\gamma_i} \\ \boldsymbol{\omega}_{\gamma_i} \end{bmatrix}^T = \begin{bmatrix} 0 & 0 & 0 & 0 & 0 & 1 \end{bmatrix}^T,$$ (19b)

$$\boldsymbol{\xi}_{\alpha_i} = \begin{bmatrix} \mathbf{p}_{\alpha_i} \times \boldsymbol{\omega}_{\alpha_i} \\ \boldsymbol{\omega}_{\alpha_i} \end{bmatrix}^T = \begin{bmatrix} 0 & 0 & 0 & 1 & 0 & 0 \end{bmatrix}^T.$$ (19c)

The spatial manipulator Jacobian ($\mathbf{J}_\Theta \in \mathbb{R}^{6 \times 6}$) is computed using the set of angles ($\Theta \in \mathbb{S}^6$) that describe the configuration of the rigid-body model as follows

$$\Theta = \begin{bmatrix} \beta_2 & \gamma_2 & \alpha_2 & \beta_3 & \gamma_3 & \alpha_3 \end{bmatrix}^T,$$ (20)

$$\mathbf{J}_\Theta = \begin{bmatrix} \boldsymbol{\xi}'_{\beta_2} & \boldsymbol{\xi}'_{\gamma_2} & \boldsymbol{\xi}'_{\alpha_2} & \boldsymbol{\xi}'_{\beta_3} & \boldsymbol{\xi}'_{\gamma_3} & \boldsymbol{\xi}'_{\alpha_3} \end{bmatrix}$$ (21)

with

$$\boldsymbol{\xi}'_{\beta_i} = \text{Ad}\left(\mathbf{T}_1^2 \dots \mathbf{T}_{i-2}^{i-1}\Big|_{l_{i-1}=0}\right)\boldsymbol{\xi}_{\beta_i},$$ (22a)

$$\boldsymbol{\xi}'_{\gamma_i} = \text{Ad}\left(\mathbf{T}_1^2 \dots \mathbf{T}_{i-1}^i\Big|_{l_i=0,\gamma_i=0}\right)\boldsymbol{\xi}_{\gamma_i},$$ (22b)

$$\boldsymbol{\xi}'_{\alpha_i} = \text{Ad}\left(\mathbf{T}_1^2 \dots \mathbf{T}_{i-1}^i\Big|_{l_i=0,\alpha_i=0}\right)\boldsymbol{\xi}_{\alpha_i},$$ (22c)

where $\text{Ad}(\mathbf{T})$ is the adjoint transformation of transformation matrix $\mathbf{T}$. The details of the above derivation can be found in [33].

APPENDIX B
OBSERVER-BASED FUSION DERIVATION

A simplified kinematics-based model is developed with a disturbance term. Furthermore, it is assumed that the dynamics of the manipulator can be approximated by a linear time-invariant model. More information on the formulation of the system dynamics and the disturbance dynamics can be found in the work by Denasi *et al.* [23]. The Kalman filter uses the model with a suitable update term to estimate state variables that cannot be measured. The Kalman filter has two phases at each sampling loop: prediction and update. Prediction is applied on the augmented system dynamics, where the system is observable. The state estimate is obtained using the discretized system dynamics as follows

$$\hat{\mathbf{x}}_{k+1|k} = \mathbf{A}_d\hat{\mathbf{x}}_{k|k} + \mathbf{B}_d\mathbf{u}(k), \tag{23}$$

where $\hat{\mathbf{x}}_{k|k}$ is the estimate of $\hat{\mathbf{x}}$ at time instant k given observations up to and including at time k. $\mathbf{u}(k)$ is the control input, $\mathbf{A}_d$ and $\mathbf{B}_d$ are the discretized terms of the augmented system. The predicted estimate of the error covariance matrix is given by

$$\mathbf{P}_{k+1|k} = cov\big(\mathbf{x}_{k+1} - \hat{\mathbf{x}}_{k+1|k}\big) = \mathbf{A}_d\mathbf{P}_{k|k}\mathbf{A}_d^T + \mathbf{Q}, \tag{24}$$

where $\mathbf{Q} \in \mathbb{R}^{3(n_d+n_p)\times 3(n_d+n_p)}$ is the covariance matrix of the process noise in the three coordinate axes, n_d and n_p are the order of the plant and disturbance dynamics, respectively. In the update phase, the state estimate is corrected with an innovation term involving the measurements.

$$\hat{\mathbf{x}}_{k+1|k+1} = \hat{\mathbf{x}}_{k+1|k} + \mathbf{K}_{k+1}\big[\mathbf{y}(k) - \mathbf{C}_d\hat{\mathbf{x}}_{k+1|k}\big], \tag{25}$$

where $\mathbf{y}(k)$ is the measurement data from the model and FBG sensors at time k and $\mathbf{K}_{k+1}$ is the optimal Kalman gain calculated as

$$\mathbf{K}_{k+1|k+1} = \mathbf{P}_{k+1|k}\big[\mathbf{C}_d\mathbf{P}_{k+1|k}\mathbf{C}_d^T + \mathbf{R}\big]^{-1}, \tag{26}$$

Here, $\mathbf{R} \in \mathbb{R}^{l\times l}$ is the covariance matrix of the measurement noise and $l = 6$ represents the number of the measurement data from the sensors. Finally, the estimate of the error covariance is updated as follows

$$\mathbf{P}_{k+1|k+1} = \big[\mathbf{I}_{(n_d+n_p)} - \mathbf{K}_{k+1}\mathbf{C}_d\big]\mathbf{P}_{k+1|k}, \tag{27}$$

where $\mathbf{I}_{(n_d+n_p)}$ is the identity matrix and $\mathbf{C}_d$ belongs to the disturbance dynamics measurement. Therefore, the estimated pose of the manipulator is obtained from the fused position ($\mathbf{p}^{\text{est}} \in \mathbb{R}^3$) and orientation ($\boldsymbol{\theta}^{\text{est}} \in \mathbb{S}^3$) computed using (25).
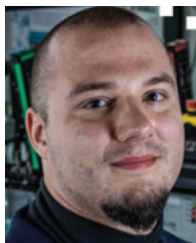
REFERENCES

[1] J. Burgner-Kahrs, D. C. Rucker, and H. Choset, "Continuum robots for medical applications: A survey," *IEEE Trans. Robot.*, vol. 31, no. 6, pp. 1261–1280, Dec. 2015.

[2] T. L. Thomas, V. K. Venkiteswaran, G. K. Ananthasuresh, and S. Misra, "Surgical applications of compliant mechanisms: A review," *J. Mechanisms Robot.*, vol. 13, no. 2, Jan. 2021, Art. no. 20801. [Online]. Available: https://doi.org/10.1115/1.4049491

[3] Z. Du, W. Yang, and W. Dong, "Kinematics modeling of a notched continuum manipulator," *J. Mechanisms Robot.*, vol. 7, no. 4, Nov. 2015, Art. no. 41017. [Online]. Available: https://doi.org/10.1115/1.4028935

[4] P. J. Swaney, P. A. York, H. B. Gilbert, J. Burgner-Kahrs, and R. J. Webster, "Design, fabrication, and testing of a needle-sized wrist for surgical instruments," *J. Med. Devices*, vol. 11, no. 1, pp. 145011–145019, 2017.

[5] K. W. Eastwood *et al.*, "Design of a contact-aided compliant notched-tube joint for surgical manipulation in confined workspaces," *J. Mechanisms Robot.*, vol. 10, no. 1, 2018, Art. no. 15001.

[6] R. J. Webster III and B. A. Jones, "Design and kinematic modeling of constant curvature continuum robots: A review," *Int. J. Robot. Res.*, vol. 29, no. 13, pp. 1661–1683, 2010.

[7] D. Trivedi, A. Lotfi, and C. D. Rahn, "Geometrically exact dynamic models for soft robotic manipulators," in *Proc. IEEE/RSJ Int. Conf. Intell. Robots Syst.*, San Diego, CA, USA, Nov. 2007, pp. 1497–1502.

[8] T. Greigarn, R. C. Jackson, T. Liu, and M. C. Çavuşoğlu, "Experimental validation of the pseudo-rigid-body model of the MRI-actuated catheter," in *Proc. IEEE Int. Conf. Robot. Autom. (ICRA)*, Singapore, Jun. 2017, pp. 3600–3605.

[9] B. S. Peters, P. R. Armijo, C. Krause, S. A. Choudhury, and D. Oleynikov, "Review of emerging surgical robotic technology," *Surg. Endoscopy*, vol. 32, no. 4, pp. 1636–1655, 2018.

[10] C. M. Heunis, J. Sikorski, and S. Misra, "Flexible instruments for endovascular interventions: Improved magnetic steering, actuation, and image-guided surgical instruments," *IEEE Robot. Autom. Mag.*, vol. 25, no. 3, pp. 71–82, Sep. 2018.

[11] C. Pappone *et al.*, "Robotic magnetic navigation for atrial fibrillation ablation," *J. Amer. College Cardiol.*, vol. 47, no. 7, pp. 1390–1400, 2006.

[12] L. B. Kratchman, T. L. Bruns, J. J. Abbott, and R. J. Webster, "Guiding elastic rods with a robot-manipulated magnet for medical applications," *IEEE Trans. Robot.*, vol. 33, no. 1, pp. 227–233, Feb. 2017.

[13] T. da Veiga *et al.*, "Challenges of continuum robots in clinical context: A review," *Prog. Biomed. Eng.*, vol. 2, no. 3, 2020, Art. no. 32003.

[14] A. Bajo and N. Simaan, "Hybrid motion/force control of multi-backbone continuum robots," *Int. J. Robot. Res.*, vol. 35, no. 4, pp. 422–434, 2016.

[15] J. Edelmann, A. J. Petruska, and B. J. Nelson, "Magnetic control of continuum devices," *Int. J. Robot. Res.*, vol. 36, no. 1, pp. 68–85, 2017.

[16] C. Shi *et al.*, "Shape sensing techniques for continuum robots in minimally invasive surgery: A survey," *IEEE Trans. Biomed. Eng.*, vol. 64, no. 8, pp. 1665–1678, Aug. 2017.

[17] Y.-L. Park *et al.*, "Real-time estimation of 3-D needle shape and deflection for MRI-guided interventions," *IEEE/ASME Trans. Mechatronics*, vol. 15, no. 6, pp. 906–915, Dec. 2010.

[18] R. J. Roesthuis, M. Kemp, J. J. van den Dobbelsteen, and S. Misra, "Three-dimensional needle shape reconstruction using an array of fiber bragg grating sensors," *IEEE/ASME Trans. Mechatronics*, vol. 19, no. 4, pp. 1115–1126, Aug. 2014.

[19] O. Al-Ahmad, M. Ourak, J. Van Roosbroeck, J. Vlekken, and E. Vander Poorten, "Improved FBG-based shape sensing methods for vascular catheterization treatment," *IEEE Robot. Autom. Lett.*, vol. 5, no. 3, pp. 4687–4694, Jul. 2020.

[20] F. Khan, A. Denasi, D. Barrera, J. Madrigal, S. Sales, and S. Misra, "Multi-core optical fibers with Bragg gratings as shape sensor for flexible medical instruments," *IEEE Sensors J.*, vol. 19, no. 14, pp. 5878–5884, Jul. 2019.

[21] T. L. Thomas, V. K. Venkiteswaran, G. K. Ananthasuresh, and S. Misra, "A monolithic compliant continuum manipulator: A proof-of-concept study," *J. Mechanisms Robot.*, vol. 12, no. 6, May 2020, Art. no. 61006. [Online]. Available: https://doi.org/10.1115/1.4046838

[22] J. Sikorski, A. Denasi, G. Bucchi, S. Scheggi, and S. Misra, "Vision-based 3-D control of magnetically actuated catheter using BigMag—An array of mobile electromagnetic coils," *IEEE/ASME Trans. Mechatronics*, vol. 24, no. 2, pp. 505–516, Apr. 2019.

[23] A. Denasi *et al.*, "An observer-based fusion method using multicore optical shape sensors and ultrasound images for magnetically-actuated catheters," in *Proc. IEEE Int. Conf. Robot. Autom. (ICRA)*, Brisbane, QLD, Australia, May 2018, pp. 50–57.

[24] J. P. Den Hartog, *Advanced Strength of Materials*. Mineola, NY, USA: Dover Publ., 1987.

[25] V. K. Venkiteswaran, J. Sikorski, and S. Misra, "Shape and contact force estimation of continuum manipulators using pseudo rigid body models," *Mechanism Mach. Theory*, vol. 139, pp. 34–45, Sep. 2019.

[26] M. Richter, V. K. Venkiteswaran, and S. Misra, "Multi-point orientation control of discretely-magnetized continuum manipulators," *IEEE Robot. Autom. Lett.*, vol. 6, no. 2, pp. 3607–3614, Apr. 2021.

[27] F. Khan, A. Donder, S. Galvan, F. R. Y. Baena, and S. Misra, "Pose measurement of flexible medical instruments using fiber Bragg gratings in multi-core fiber," *IEEE Sensors J.*, vol. 20, no. 18, pp. 10955–10962, Sep. 2020.

[28] N. Shahriari, W. Heerink, T. Van Katwijk, E. Hekman, M. Oudkerk, and S. Misra, "Computed tomography (CT)-compatible remote center of motion needle steering robot: Fusing CT images and electromagnetic sensor data," *Med. Eng. Phys.*, vol. 45, pp. 71–77, Jul. 2017.

[29] M. Kaya *et al.*, "A multi-rate state observer for visual tracking of magnetic micro-agents using 2d slow medical imaging modalities," in *Proc. IEEE/RSJ Int. Conf. Intell. Robots Syst. (IROS)*, Madrid, Spain, Oct. 2018, pp. 1–8.

[30] X. Hu, A. Chen, Y. Luo, C. Zhang, and E. Zhang, "Steerable catheters for minimally invasive surgery: A review and future directions," *Comput. Assisted Surg.*, vol. 23, no. 1, pp. 21–41, 2018.

[31] F. H. Wittkampf, E. F. Wever, R. Derksen, H. Ramanna, R. N. Hauer, and E. O. R. de Medina, "Accuracy of the LocaLisa system in catheter ablation procedures," *J. Electrocardiol.*, vol. 32, pp. 7–12, 1999. [Online]. Available: https://doi.org/10.1016/S0022-0736(99)90026-2

[32] F. Khan, D. Barrera, S. Sales, and S. Misra, "Curvature, twist and pose measurements using fiber Bragg gratings in multi-core fiber: A comparative study between helical and straight core fibers," *Sensors Actuators A Phys.*, vol. 317, Jan. 2021, Art. no. 112442.

[33] R. M. Murray, Z. Li, and S. S. Sastry, *A Mathematical Introduction to Robotic Manipulation*. Boca Raton, FL, USA: CRC Press, 1994.

G. K. Ananthasuresh received the bachelor's degree in mechanical engineering from IIT-Madras, the master's degree in mechanical engineering from the University of Toledo, and the Ph.D. degree in mechanical engineering from the University of Michigan, Ann Arbor. He is currently a Professor of Mechanical Engineering and the Dean of the Division of Mechanical Sciences with the Indian Institute of Science, Bengaluru. In addition to research output of about 300 journal and conference publications and 16 patents, his research group has spun off four startups. He is a coauthor or a sole author of two textbooks, five edited books, and 17 book chapters. His principal research interests are compliant mechanisms and topology optimization with applications in microelectromechanical systems, biomechanics of cells, biomedical devices, and microrobotics. He and his students have been recognized with 14 best paper awards and ten design prizes. His work is recognized with the National Science Foundation (USA) Early Career Award, the Society of Automotive Engineers Ralph R. Teeter Educational Award (USA) as well as the Swarnajayanthi Fellowship, the Shanti Swarup Bhatnagar Prize, and the Abdul Kalam Technology Innovation National Fellowship from the Government of India.

Theodosia Lourdes Thomas (Graduate Student Member, IEEE) received the bachelor's degree in engineering design and the master's degree in biomedical design from the Indian Institute of Technology Madras, Chennai, India, in 2018. She is currently pursuing the Ph.D. degree in biomechanical engineering with the Surgical Robotics Laboratory, University of Twente, The Netherlands. Her doctoral research is focused on design and control of magnetically-actuated compliant continuum manipulators for minimally invasive surgery.

Venkatasubramanian Kalpathy Venkiteswaran (Member, IEEE) received the Ph.D. degree in mechanical engineering from The Ohio State University, Columbus, OH, USA, in 2017. He is currently an Assistant Professor with the Department of Biomechanical Engineering, University of Twente, The Netherlands. Prior to that, he was a Postdoctoral Fellow with the Surgical Robotics Laboratory, University of Twente for two years. His research interests include design of soft robots and flexible devices with a focus on medical applications.

Jakub Sikorski (Member, IEEE) received the M.Eng. degree in biomedical engineering from the University of Glasgow, Glasgow, U.K., in 2015, and the Ph.D. degree in biomechanical engineering from the University of Twente, Enschede, The Netherlands, in 2020. From 2020 to 2022, he worked as a Postdoctoral Researcher with the Surgical Robotics Laboratory, University of Twente.

Sarthak Misra (Senior Member, IEEE) received the master's degree in mechanical engineering from McGill University, Montreal, QC, Canada, in 2001, and the Ph.D. degree in mechanical engineering from Johns Hopkins University, Baltimore, MD, USA, in 2009. He is currently a Full Professor with the Department of Biomechanical Engineering, University of Twente, Enschede, The Netherlands, and with the Department of Biomedical Engineering, University of Groningen and University Medical Center Groningen, Groningen, The Netherlands. Prior to commencing his doctoral studies, he was a Dynamics and Controls Analyst with the International Space Station Program. His research interests include surgical robotics and medical microrobotics. He was the recipient of the European Research Council Starting, Proof-of-Concept, and Consolidator Grants and the Netherlands Organization for Scientific Research VENI and VIDI Awards. He is the Co-Chair of the Robotics and Automation Society Technical Committee on Surgical Robotics and the International Federation of Automatic Control Technical Committee on Biological and Medical Systems.